Journal of Molecular Structure 1353 (2026) 144689

Contents lists available at ScienceDirect

Journal of Molecular Structure

journal homepage: www.elsevier.com/locate/molstr

Comprehensive analysis of triazolothiadiazole derivative: From synthesis and crystal structure to quantum chemical and molecular simulation studies on JAK2 protein

D.C. Vinay Kumar [a], B.S. Chethan [b], S. Neetha [a], Darshini Gowda [c], V. Shalini [d,f], T.N. Lohith [a], K.S. Rangappa [d,*], N.K. Lokanath [e,*]

[a] Department of Physics, The National Institute of Engineering, Mysuru, Karnataka 570 008, India
[b] Department of Physics, Sri Siddhartha Institute of Technology, SSAHE, Tumakuru, Karnataka 572105, India
[c] Department of Chemistry, IDSG Government First Grade College, Chikmagalur, Karnataka 577102, India
[d] Institute of Excellence, Vijnana Bhavan, University of Mysore, Manasagangotri, Mysuru, Karnataka 570006, India
[e] Department of Studies in Physics, University of Mysore, Manasagangotri, Mysuru, Karnataka, 570 006, India
[f] Department of Chemistry, Mysore University School of Engineering, University of Mysore, Manasagangitri, Mysuru, Karnataka, 570006, India

ARTICLE INFO

Keywords:
Triazolothiadiazole derivative
Single-crystal X-ray diffraction
Non-covalent interactions
Hirshfeld surface analysis
Density functional theory
Docking analysis
JAK2
Molecular dynamics simulations

ABSTRACT

In the present work, a triazolothiadiazole derivative *4-(3-(pyridin-4-yl)-7H-[1,2,4]triazolo[3,4-b][1,3,4]thiadiazin-6-yl)phenol* **[PTTP]** was synthesized and systematically investigated through experimental and computational approaches to establish the structural features and biological potential. The synthesized compound was characterized by standard spectroscopic techniques (LCMS, FT-IR, NMR, and UV–Vis), confirming the molecular frameworks. Single-crystal X-ray diffraction revealed that the crystal is stabilized by intermolecular interactions of the type C13B-H13B···O1 (2.444 Å) and O1-H1···N5B (1.949 Å). The influence of these non-covalent interactions was further examined using Hirshfeld surface analysis, providing a quantitative understanding of molecular packing contributions. Density functional theory (DFT) simulations at the B3LYP/6–311++*G*(d,p) level accurately predicted molecular geometry and matched experimental results. The HOMO-LUMO energy gap of the compound is 3.968 eV. The docking analysis between JAK2 inhibitors and PTTP compound showed docking score of -9.5 kcal/mol, indicating favorable binding affinity. The docking results were further validated through molecular dynamics (MD) simulations, which demonstrated the stability and dynamic behavior of the protein–ligand complexes under physiological conditions.

1. Introduction

Triazolothiadiazole derivatives constitute an important class of fused heterocycles, in which the 1,2,4-triazole ring is condensed with a 1,3,4-thiadiazole moiety, creating a rigid and electron-rich bicyclic pharmacophore [1–3]. The presence of multiple heteroatoms (N and S) within the scaffold imparts high electron density and enables hydrogen bonding, dipole–dipole contacts, π–π stacking, and metal coordination, thereby enhancing their ability to interact with diverse biomolecular targets. Structure–activity relationship (SAR) studies suggest that electron-donating substituents (–OH, –OCH_3, –NH_2) on aromatic/heteroaromatic side chains improve hydrogen bonding with active-site residues, while halogen substitution (–Cl, –F, –Br) enhances lipophilic contacts and improves bioavailability [4,5]. Moreover, the fused triazole unit often acts as a bioisostere of amide or purine groups, favoring recognition by ATP-binding enzymes, whereas the thiadiazole moiety contributes to enhanced planarity, aromatic stabilization, and sulfur-mediated interactions within protein cavities. With respect to *Janus tyrosine kinase 2* (JAK2), a critical non-receptor tyrosine kinase implicated in cytokine signaling and inflammatory pathways, triazolothiadiazole derivatives display promising inhibitory potential [6,7]. Triazolothiadiazole derivatives have emerged as highly versatile scaffolds in medicinal chemistry due to their heteroatom-rich fused framework, which allows diverse interactions with biological targets. They exhibit broad antimicrobial properties, showing significant inhibition against bacterial and fungal strains through interference with

* Corresponding authors.
E-mail addresses: rangappaks@ioe.uni-mysore.ac.in (K.S. Rangappa), lokanath@physics.uni-mysore.ac.in (N.K. Lokanath).

https://doi.org/10.1016/j.molstruc.2025.144689
Received 28 August 2025; Received in revised form 14 October 2025; Accepted 8 November 2025
Available online 8 November 2025

microbial enzymes and DNA synthesis. Several derivatives demonstrate anticancer activity by targeting kinases, tubulin, or DNA, with some acting as potent inhibitors of VEGFR-2 and *JAK2* [8–10]. Their anti-inflammatory and analgesic effects are linked to the inhibition of cyclooxygenase isoforms and modulation of pro-inflammatory cytokines, while certain compounds also display anticonvulsant properties through interactions with GABAergic and glutamatergic systems [11–14]. In the field of metabolic disorders, triazolothiadiazoles show promising antidiabetic activity via inhibition of α-glucosidase and aldose reductase, thereby controlling hyperglycemia and preventing secondary complications. Additionally, their electron-rich structure contributes to notable antioxidant activity, protecting cells from oxidative stress. Beyond these, they act as inhibitors of enzymes such as tyrosinase, urease, carbonic anhydrase, and cholinesterases, expanding their applications to neurodegenerative, dermatological, and gastric disorders. Collectively, these properties highlight triazolothiadiazoles as privileged scaffolds for the rational design of novel therapeutics across oncology, infectious diseases, neurology, endocrinology, and inflammatory conditions [15,16]. Ineffective hematopoiesis and bone marrow fibrosis are hallmarks of myelofibrosis, a clonal myeloproliferative disease often referred to as agnogenic myeloid metaplasia or primary myelofibrosis [17–19]. The US Food and Drug Administration (FDA) has authorized pacritinib (CTI Biopharma), an oral kinase inhibitor that targets JAK2, to treat myelofibrosis (MF) [20].

Molecular docking and computational studies have shown that these derivatives can occupy the ATP-binding cleft of JAK2, establishing hydrogen bonds with hinge-region residues, while the sulfur and nitrogen atoms of the triazolothiadiazole core contribute to polar interactions with amino acids, which are essential for kinase stabilization. Additionally, hydrophobic substituents attached to the scaffold extend into the hydrophobic back pocket, interacting with residues, thereby enhancing binding affinity [21,22]. Such dual interaction modes—polar anchoring via heteroatoms and hydrophobic complementarity *via* aromatic substituents—highlight the versatility of this scaffold in targeting JAK2. Collectively, these properties position triazolothiadiazole derivatives as attractive leads for the development of selective JAK2 inhibitors, offering therapeutic potential in the management of myeloproliferative disorders, autoimmune diseases, and inflammatory conditions [23].

In the present study, a comprehensive investigation of triazolothiadiazole derivatives was undertaken, integrating both experimental and computational approaches to establish their structural and biological significance. The molecular architecture of the compounds was unambiguously determined through single-crystal X-ray diffraction analysis, providing precise insights into their three-dimensional geometry and crystal packing features. To complement the experimental findings, density functional theory (DFT) calculations were employed to probe the electronic properties, structural stability, and global reactivity descriptors at the quantum chemical level [24]. Furthermore, to evaluate their pharmacological relevance, molecular docking studies were performed against the Janus tyrosine kinase 2 (JAK2) protein, a validated therapeutic target in inflammatory and proliferative disorders, in order to predict binding affinities and key interaction profiles [25]. To gain deeper insights into the stability and conformational dynamics of the protein–ligand complexes under physiological conditions, molecular dynamics (MD) simulations were carried out, providing valuable information on binding stability, flexibility, and intermolecular interactions over time. Collectively, this integrated strategy establishes a strong foundation for understanding the structural attributes, electronic features, and JAK2-inhibitory potential of triazolothiadiazole derivatives, thereby supporting their further development as promising therapeutic candidates [26].

Table 1
Crystal data and structure refinement details of PTTP.

Parameter	Value
CCDC deposit No.	2203,513
Empirical formula	$C_{15}H_{11}N_5OS$
Formula weight	309.35
Temperature (K)	293
Wavelength (Å)	0.71073
Crystal system, space group	Monoclinic, $P2_1/c$
Unit cell dimensions	$a = 15.534(4)$ (Å) $b = 14.120(4)$ (Å) $c = 12.585(5)$ (Å) $\beta = 101.508(7)^\circ$
Volume Å^3	2704.9(15)
Z	8
Density (ρ) (calculated) in g/cm^{-3}	1.519
Absorption coefficient (mm^{-1})	0.249
F_{000}	1280
θ range for data collection	6.082° to 54.97°
Index ranges	$-20 \le h \le 20$ $-7 \le k \le 18$ $-14 \le l \le 16$
Reflections collected	15,334
Independent reflections	6189 [$R_{int} = 0.0808$, R sigma = 0.0984]
Refinement method	Full matrix least-squares on F^2
Data/restraints/parameters	6189/0/405
Goodness-of-fit on F^2	1.030
Final [$I > 2\sigma(I)$]	$R_1 = 0.0656$, $wR_2 = 0.1193$
R indices (all data)	$R_1 = 0.1417$, $wR_2 = 0.1442$
Largest diff. peak and hole	0.29 and −0.30 e Å^{-3}

2. Materials and methods

2.1. Experimental details

All the reagents and solvents were purchased from Sigma-Aldrich and were used without further purification. The liquid chromatography-mass spectrometry (LC-MS) was recorded using Xevo G2-XS QTof system, Waters, USA. NMR spectra were recorded on Agilent NMR spectrometer at 400 MHz for ^{1}H NMR and at 100 MHz for ^{13}C NMR. The signals are abbreviated as: singlet, s; doublet, d; triplet, t; doublet-doublet, dd; multiplet, m; DMSO-d_6 and $CDCl_3$ are used as a solvent, and chemical shifts (δ) are reported in parts per million (ppm) relative to Tetramethylsilane (TMS). UV–vis spectra were recorded with Beckman Coulter DU 730 UV–vis Spectrophotometer between 450 and 800 nm. The synthesized compound Fourier-transform infrared (FT-IR) spectra was recorded using a Perkin Elmer FT-IR C94012 Spectrophotometer from 450 to 4000 cm^{-1}. The X-ray diffraction intensity data were collected using Rigaku XtaLAB mini diffractometer with Mo-Kα radiation (λ = 0.71073 Å).

2.1.1. X-ray crystallography

A good quality light brown single crystal was isolated from the solution using a polarizing microscope, to check for its size, shape and defect free. The crystal was mounted on the goniometer and X-ray intensity data were collected at 293 K with a Rigaku XtaLAB mini diffractometer equipped with a charge-coupled device detector X-ray diffractometer with graphite-monochromated X-ray generator operating at 50 kV, 12 mA, and Mo-Kα radiation of wavelength 0.71073 Å. The unit cell dimensions, crystal orientation, and Bravais lattice type were elucidated by indexing the initial reflection frames (at 3 s exposure). The intensity data were collected with χ fixed at 54° and for different angular settings of ω and φ (0° and 360°), keeping the scan width of 0.5° with an exposure time of 3 s, and the sample to detector distance was fixed to 50 mm. A complete data set was processed using *CrystalClear-SM EXPERT software* [27]. The structure was solved by direct methods. All the non-hydrogen atoms were revealed in the first difference Fourier map itself and refined by the full-matrix least-squares method on F^2 using

SHELXS and *SHELXL* [28,29] programs as implemented in *OLEX2 software*. The non-hydrogen atoms of the molecules were identified and anisotropically assigned without any positional constraints. All hydrogen atoms were located in the model at geometrically calculated positions and refined using a riding model on their respective parent atom. Crystallographic data and structure refinement parameters were summarized in Table 1. Crystal structure geometry calculations such as bond lengths, bond angles, and torsion angles were carried out using the *PLATON* program [30]. The *ORTEP* and packing diagrams were generated using *MERCURY* 4.2.0 software [31].

2.1.2. Hirshfeld surface analysis

The short contacts, inter-molecular interactions, crystal packing, inter-nuclear distances, and angles in the crystal structure were visualized and analyzed using Hirshfeld surfaces, d_{norm} (normalized contact distance), d_i, d_e and their relative 2D fingerprint plots were drawn using *CrystalExplorer 17.5* software [32,33]. The d_i (inside) and d_e (outside) represent the distances to the Hirshfeld surface from the selected molecule concerning the relative Van der Waals radii. The fingerprint plots quantify the inter molecular interactions of the structure. The Hirshfeld surfaces and their associated 2D fingerprint plots (FPs) were generated for the title compound using the crystallographic information file (CIF) [34]. Graphical plots of the 3D molecular Hirshfeld surfaces were mapped over the d_{norm} enabling the identification of the region of particular importance to explore the inter-molecular interactions.

2.2. Density functional theory

The quantum chemical calculations were performed by density functional theory (DFT) based on B3LYP/6–311+G(d,p) basis set [35, 36] approximation in the *Gaussian 16* to optimize the compound [37]. The GaussView 6.0.16 [38] is used to visualize the output results. The frontier molecular orbital (FMO) analysis, electrostatic potential surface, and electronic properties such as energies, HOMO and LUMO orbitals, HOMO-LUMO energy gap (ΔE), ionization potential (I), electron affinity (A), global hardness (η), electronegativity (χ), electronic chemical potential (μ), electrophilicity (ω) and chemical softness (S) were estimated using the $E_{HOMO,}$ and E_{LUMO} energies [39]. Natural bond orbital study is carried out to understand the stabilization and hyper conjugation interactions exhibited by the compound by employing the NBO program [40] in *Gaussian 16* software.

2.2.1. QTAIM

QTAIM (quantum theory of atoms in molecule) analysis was performed using *Multiwfn* software-3.6 [41] on the wave function generated by density functional theory calculations. To get further insight towards the understanding of the various intra and intermolecular interactions exhibited by the titled compound Bader's Quantum theory of atoms in molecules was employed [42,43]. The topological parameters such as the electron density ($\rho(r)$), the Laplacian of electron density ($\nabla^2\rho$), local potential energy density ($V(r)$), and kinetic energy density ($G(r)$) for various intra molecular interactions at the bond critical points (BCPs) of the compound were calculated.

2.3. Molecular docking

The molecular docking study of the PTTP molecule with JAK2 protein was carried out using MGL tools 1.5.6 with *AutoDock Vina* [44]. The three-dimensional structure of *JAK2* (PDB ID: 4C61) was downloaded from the protein data bank in PDB format. Using the *AutoDock* Tools, polar hydrogen atoms were added to the energy minimized protein, and Kollman charges were added to the receptor molecule after the hetero-atoms, including water molecules, were removed. Rotatable bonds were permitted for all other bonds. The binding sites were defined using grid center, and it was set to −0.964, −0.060, and 33.242 and grid sizes of 56, 64, and 60 Å each for *X, Y*, and *Z*, respectively. Through the command script provided by developers, the docking simulations were performed with *AutoDock Vina*. The binding affinity of the novel ligand was observed as a negative score with the unit of kcal/mol. The protein-ligand interactions were visualized, and the binding sites were analyzed using *Biovia Discovery Studio* 2019 Client visualizer [45].

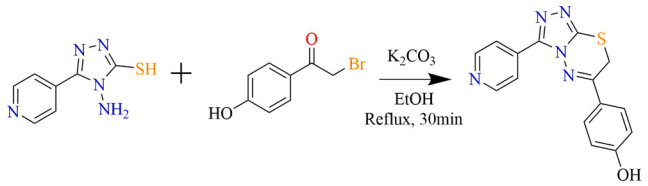

Fig. 1. Reaction pathway for the synthesis of the PTTP compound.

2.4. Molecular dynamics simulation

Desmond molecular dynamic simulation was carried out on a 64-bit Ubuntu 20.04 platform in a Dell Precision 7820 equipped with an Intel Xeon Gold (80core), 512 GB RAM, and a 24 GB Quadro RTX-6000 Nvidia GPU. MDSs experiments for ligand PTTP against *JAK2* protein were carried out to investigate its dynamics in a given simulated system [46]. Using the system-builder option, the TIP3P (transferable intermolecular potential with three points) water model was integrated into the docked protein-ligand complex in an orthorhombic periodic boundary of the box under solvated circumstances [47]. The system was neutralized by Na+ ions (50.655 mM, charge +447), and Cl- (53.488 mM, charge −472) were added to it. Furthermore, MDS investigations were performed using a periodic boundary condition in the number of atoms, pressure, and temperature (NPT) ensemble, at 310 K and 1 atmospheric pressure, and then relaxed using the Desmond program's default relaxation methodology. The simulation job was carried out for 200 ns for JAK2 protein [48].

3. Results and discussions

3.1. Synthesis

All the reagents and solvents are commercially purchased from Sigma-Aldrich and were used without further purification. The equimolar amount of *4-amino-5-(pyridin-4-yl)-4H-1,2,4-triazole-3-thiol* and *2-bromo-1-(4-hydroxyphenyl)ethan-1-one* were taken in an RB and a small amount of K_2CO_3 is added as a base to the mixture. Then mixture resulting solution was stirred for 30 min in ethanol solvent at 70° C, and then it is allowed to cool to room temperature. Later ammonium hydroxide is added to the reaction mixture, followed by the addition of ice-cold water resulting in the precipitation of the product. Then the solid product is dried, and purified by column chromatography over silica gel (60–120 mesh) using hexane and ethyl acetate mixture in appropriate ratios as eluent, to obtain the final compound *4-(3-(pyridin-4-yl)-7H-[1,2,4]triazolo[3,4-b][1,3,4]thiadiazin-6-yl)phenol* **[PTTP]**. The compound is dissolved in various solvents and kept for slow evaporation. After a few days light yellow crystals were obtained in the combination of methanol and DCM solvent. Then the synthesized compound is confirmed through liquid chromatography-mass spectrometry (LC-MS) recorded on MS Waters SynaptG2 spectrometer (Xevo G2 XS Qtof) system (Fig. S-1). The scheme of the synthesis of the PTTP compound is given in Fig. 1.

3.2. Spectroscopic characterizations

Yield: 85–90 %, LC-MS: 310.01 (Fig. S1). The ^{1}H NMR spectra of the synthesized compound showed two singlets and four doublets, ^{1}H NMR (DMSO-d6) δ ppm: 11.59 (s, OH), 8.659 (d, J = 2.4 Hz, 2H), 7.909 (s, 1H), 7.741 (d, J = 8 Hz, 2H), 6.745 (d, J = 8 Hz, 2H), 4.243 (s, 1H)

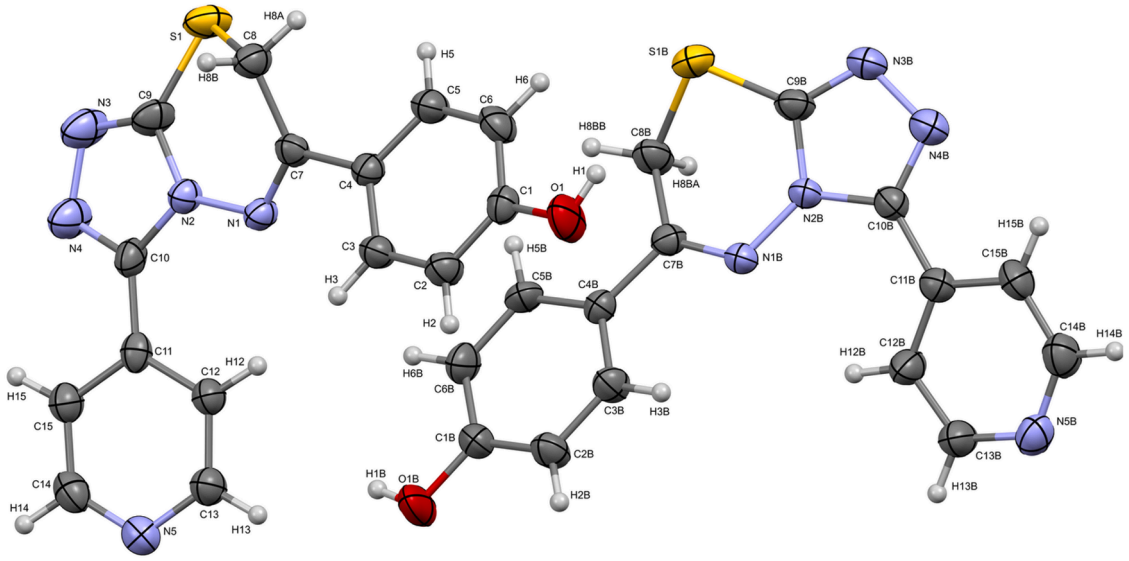

Fig. 2. The *ORTEP* of the PTTP compound drawn at 50 % probability.

(Fig. S2). The ^{13}C NMR (DMSO-d_6) δ ppm: 22.53, 116.51, 117.08, 120.87, 121.26, 121.86, 129.33, 130.44, 133.36, 144.08, 149.24, 150.36, 150.57, 156.48, 164.64 (Fig. S3).

The FT-IR spectroscopy for the PTTP compound was used for the detection of functional groups of the synthesized PTTP compound, the recorded spectrum is shown in Fig. S4(a). The vibrational bands of C—N group stretching vibrations was observed at 1270, 1364, 1427 cm^{-1}, and 1258, 1394, 1436 cm^{-1} experimental and theoretical respectively. Further various C—H groups vibrations were observed at 681, 775, 795, 1028, 1080 cm^{-1} (experimental) and 660, 765, 796, 1047, 1100 cm^{-1} (theoretical), out-plane bending vibrations, in-plane bending vibrations, stretching vibrations, respectively. The 1,2,3-triazole shows both the symmetric and asymmetric CH stretching modes obtained at 3152 cm^{-1} (experimental) and 3193 cm^{-1} (theoretical). The OH stretching vibrations were recorded at 3152, 3246, 3299, and 3825 cm^{-1} experimentally, for the DFT method while the O—H stretching band was observed at 3193, 3276, 3265, and 3855 cm^{-1} in FT-IR spectrum for PTTP compound.

UV-visible spectral analysis was performed to study the electron transition in the molecule. The maximum absorption wavelength (λ_{max}) was observed at 334 nm, indicating the π-π* transition. The DFT calculations show the maximum absorption peak at 315 nm (Fig. S4(b)).

3.3. X-ray crystallography studies

3.3.1. Crystal structure description of compound

The defect-free, needle-shaped yellow color single crystal of PTTP compound ($C_{15}H_{11}N_5OS$) with dimension 0.18×0.20×0.22 mm was selected for the single crystal X-ray diffraction data collection at 293 K. The structural analysis inferred that the compound crystallizes in a monoclinic crystal system with $P2_1/c$ space group forming a dimer of the PTTP molecule. Constitutional isomers of the two molecules that make up the dimer, which are bound in the solid state by dipole-dipole and dispersion interactions. The unit cell of dimer compound PTTP comprises eight molecules ($Z = 8$). The asymmetric unit of the compound contains two symmetry-independent molecules ($Z' = 2$), with the unit cell parameters $a = 15.534(4)$ Å, $b = 14.120(4)$ Å, $c = 12.585(5)$ Å, $\alpha = \gamma = 90°$, $\beta = 101.50(7)°$. The three-dimensional structure of the dimer PTTP molecule was solved by direct method and refined using full-matrix least-squares on F^2 converging to a residual value of 0.0656 with a goodness of fit 1.030. The crystal structure refinement parameters are summarized in Table 1. The *ORTEP* of the compound drawn at 50 % probability is given in the Fig. 2.

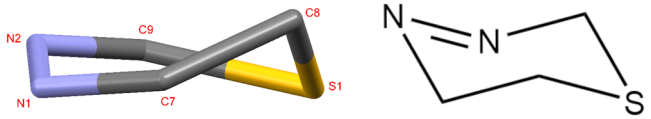

Fig. 3. The puckering of 1,3,4-thiadiazine ring (C9/N2/N1-C7/C8/S1) with screw-boat conformation.

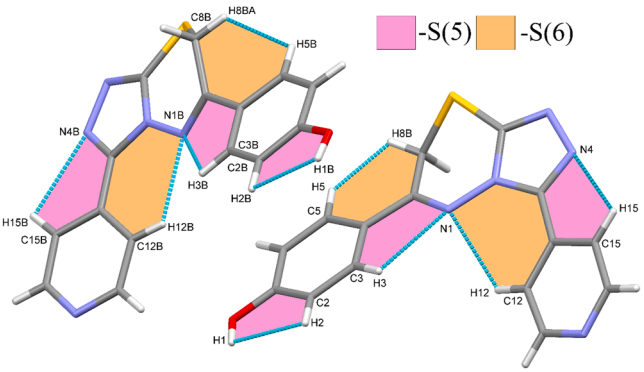

Fig. 4. Intramolecular interactions leading to the formation of the self-motifs *S* (5) and *S*(6).

The crystal packing of the PTTP molecule along the crystallographic *c*-axis is as shown in Fig. S5. The pyridine moiety and phenol ring systems in the compound are bridged by triazole and thiadiazine moiety. The dihedral angle between the phenol ring (C1/C2/C3/C4/C5/C6/Br1) (C1B/C2B/C3B/C4B/C5B/C6B/O1B) and pyridine moiety (C11/C12/C13/C14/C15/N5) (C11B/C12B/C13B/C14B/C15B/N5B) for both the molecules in the dimer are found to be 27.87° and 21.31° respectively, indicating the nonplanarity of the molecule (Fig. S6).

The 1,3,4-thiadiazine ring (C9/N2/N1-C7/C8/S1) (C9B/N2B/N1BC7B/C8B/S1B) are puckered in the molecular structure with the parameters of $Q = 0.526(3)$, $\theta = 115.1(3)°$, and $\varphi = 208.6(4)°$, and both the system adopts a screw-boat conformation (Fig. 3). The crystal structure is stabilized by C—H···N and C—H···H type intramolecular hydrogen bond interactions, resulting in the formation of planar five-membered *S*(5) and six-membered *S*(6) self-motifs (Fig. 4). The intermolecular classical and non-classical hydrogen bond interactions such as

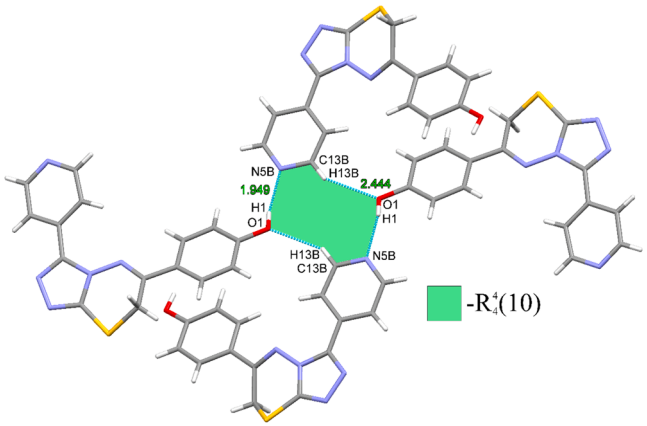

Fig. 5. The intermolecular classical and non-classical hydrogen bond interactions such as C13B-H13B···O1 and O1-H1···N5B forming $R_4^4(10)$ supramolecular cyclic synthon.

Table 2
The hydrogen bond geometry of PTTP compound.

D-H···A (Å)	D-H (Å)	H···A (Å)	D···A (Å)	D-H···A (Å)
O1-H1···N5B [(i)]	0.82	1.95	2.690(4)	150
O1B-H1B···N5 [(ii)]	0.82	1.97	2.740(4)	157
C8B-H8BA···N3[(ii)]	0.97	2.46	3.311(4)	146
C8-H8A···S1B[(iv)]	0.98(3)	2.86(3)	3.759(4)	153(2)
C8-H8B…N3B[(v)]	0.91(4)	2.52(4)	3.346(5)	151(3)
C12-H12…N1*	0.93	2.48	3.060(5)	121
C12B-H12B…N1B*	0.93	2.35	2.982(4)	125
C13B-H13B…O1[(vi)]	0.93	2.44	3.235(4)	143
C14B-H14B…O1B[(vii)]	0.93	2.46	3.053(4)	122

* Intra, symmetry code: (i)1-x,-y,-z ; (ii) 1-x,−1/2 + y,3/2-z; *(iii)-x,-y,1-z;*. *(iv) -x,1/2 + y,1/2-z; (v) -x,-y,-z; (vi) x,y,z; (vii) x,y,−1 + z.*

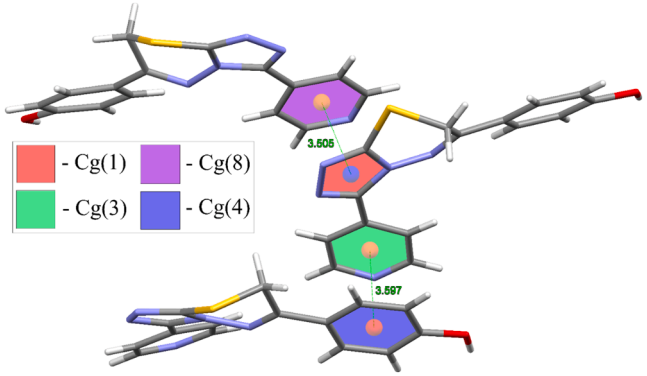

Fig. 6. The π···π stacking moieties involved in the *Cg*···*Cg* interactions exhibited by the PTTP molecule.

C13B-H13B···O1 (2.444 Å) and O1-H1···N5B (1.949 Å) respectively, connect four molecules at the inversion center to form a $R_4^4(10)$ supramolecular cyclic synthon (Fig. 5). The majority of the interactions were observed due to the C—H···N intermolecular hydrogen bond interaction play a vital role in stabilizing the molecular structure, the hydrogen bond geometry of the titled compound is provided in Table 2.

The crystal structure exhibits various π···π interactions such as, *Cg*(1)···*Cg*(8) (3.505(2) Å) between the triazole moiety (*Cg*(1): N2/C9/N3/N4/C10), pyridine ring (*Cg*(8): N5B/C13B/C12B/C11B/C15-B/C14B), *Cg*(3)···*Cg*(4) (3.597(3) Å) and between the pyridine ring (*Cg*(3): N5/C13/C12/C11/C15/C14) and phenol ring (*Cg*(4): C1/C2/C3/C4/C5/C6) respectively, to form a 1D infinite *zig-zag* chain, as shown in Fig. 6. The corresponding geometrical parameters for the π···π stacking moieties involved in the *Cg*···*Cg* interactions are given in Table 3 contribute towards the stabilization of the crystal structure.

Table 3
Geometrical parameters for the π-stacking moieties involved in the π···π interactions in compound.

Rings (I) …(J)	Distance (RC) (Å)	α (°)	β (°)	γ (°)	*Cg*I_Perp (Å)	*Cg*J_Perp (Å)
Cg(1)… *Cg*(8)[(i)]	3.505(2)	0 8.33 (16)	14.9	18.8	3.318(12)	3.387(12)
Cg(3)… *Cg*(4)[(ii)]	3.597(3)	2.72 (18)	15.4	18.1	3.418(15)	3.467(15)
Cg(4)… *Cg* (9)[(iii)]	4.014(3)	7.33 (17)	22.9	27.4	3.564(16)	3.697(14)
Cg(9)… *Cg* (6)[(iv)]	4.041(2)	12.36 (18)	27.1	29.1	3.531(14)	3.595(14)

Symmetry codes: (i) *x,y,*1 + *z*; (ii) *x,*1/2-*y,*1/2-*z*; (iii)*x, y, z*; (iv) *x,*−1/2-*y,*1/2 + *z*:

RC- Centroid distance between ring centroid I and J.
α- Dihedral angle between mean planes I and J.
β- Angle between the centroid vector Cg(I)···Cg(J) and the normal to the plane (I).
γ- Angle between the centroid vector Cg(I)···Cg(J) and the normal to the plane (I).
CgI_Perp- vertical distance from ring centroid I to ring *J*.
CgJ_Perp- vertical distance from ring centroid *J* to ring *I*.

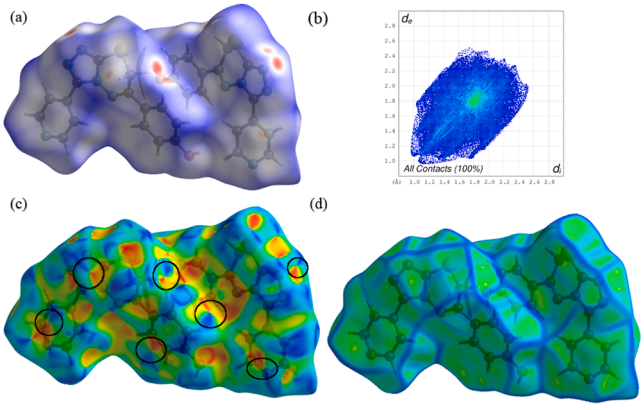

Fig. 7. (a) The dnorm mapped Hirshfeld surface, (b) 2D fingerprint plot, (c) shape index, and (d) curvedness of PTTP molecule.

3.3.2. *Hirshfeld surface analysis*

Hirshfeld surface analysis was used in a thorough examination to visualize and comprehend the intermolecular interactions in the crystals. The Hirshfeld surface mapped over dnorm and shape index of the PTTP compound was generated with a transparent surface, allows identifying the different regions that contribute to significant interactions (Fig. 7(a)). The potential short intermolecular interactions, C5-H5· · ·N3B···C8-H8B (2.664 Å and 2.523 Å), C8B-H8BA···N3 (2.463 Å), O1-H1···N5B (1.949 Å) and C13B-H13B···O1 (2.444 Å) were observed in the PTTP molecule, which are shorter than vdW separation indicated by bright red circular spots on the dnorm, which are in corroboration with the XRD results. Further, to know the percentage contribution of each type of contact to the total Hirshfeld surface areas are quantified using 2D fingerprint plots (expanded mode), and revealed that, H···H (31.8 %), N···H/H···N (22.8 %), H···S/S···H (8.2 %), C···C (8.2 %), C···H/H···C (7.7 %), and C···N/N···C (6.5 %) as shown in the Fig. 7 (b). The H···H interactions are the major contributor as compared to that of other interactions.

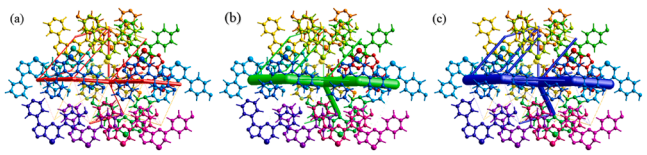

Fig. 8. The graphical representation of energy frameworks of the PTTP compound along the *c*-axis: (a) Coulomb interaction energy (red color), (b) dispersion energy (green color), and (c) total interaction energy (blue color).

3.3.3. *Shape index and curvedness*

The red and blue triangles shown on the shape index map reveals the π···π stacking weak interactions, as shown in the Fig. 7(c). The curvedness determines the shape of the molecular surface area as well as the presence of π···π stacking interactions as flat green patches on the curvedness surface (Fig. 7(d)). This feature effectively depicts the contact faces between surfaces and provides insight into the molecular packing due to the interactions between the centroids in the crystal structure.

Table 4
The interaction energies of the PTTP molecule with its corresponding geometry.

Color codes	N	Sym.op	R	E_{ele}	E_{pol}	E_{dis}	E_{rep}	E_{tot}
	1	-x, -y, -z	7.61	-7.7	-2	-39.4	26.2	-27.7
	1	-x, y+1/2, -z+1/2	13.40	-0.7	-0.1	-0.3	0	-1
	1	-x, -y, -z	16.24	0.8	0	-0.2	0	0.6
	1	x, -y+1/2, z+1/2	14.68	1.9	-0.1	-0.9	0	1.2
	1	-x, -y, -z	10.05	-7.6	-0.6	-5.3	7.9	-8.2
	1	-x, -y, -z	7.52	-3.8	-0.4	-3.6	0	-7.4
	1	x, -y+1/2, z+1/2	9.53	-25.1	-7.4	-16.5	23.6	-31.8
	1	x, y, z	9.33	-23.2	-7.4	-18	24	-30.9
	1	-x, -y, -z	7.86	6	-4.6	-22	22	-2.6
	1	-x, y+1/2, -z+1/2	13.24	0.8	-0.1	-0.6	0	0.2
	1	-x, -y, -z	17.28	-0.2	-0.1	-0.5	0	-0.6
	1	-x, -y, -z	7.61	-3.7	-5.1	-26	11	-23.5
	1	x, -y+1/2, z+1/2	19.37	0.7	0	-0.1	0	0.7
	1	-x, y+1/2, -z+1/2	9.65	-2.9	-0.4	-2.7	0	-5.7
	1	x, y, z	7.58	-5.4	-2.7	-48.8	33	-29.8
	2	x, y, z	12.59	-4.3	-0.4	-6.9	0	-10.9
	2	x, -y+1/2, z+1/2	7.17	-15.7	-3.8	-52.1	31.8	-45.2
	1	x, y, z	12.92	-37.5	-16.2	-11.1	0	-61.4
	1	x, -y+1/2, z+1/2	8.75	0.6	-3.2	-19.5	12.5	-11
	1	x, y, z	12.58	-39.2	-16.7	-11.7	0	-64
	1	-x, -y, -z	9.5	2.1	-1.1	-7.6	2.6	-3.6

N- Number of pairs, R- distance between molecular centroids, Symm.op- symmetry operation relating that particular colour-coded molecule with the center molecule.

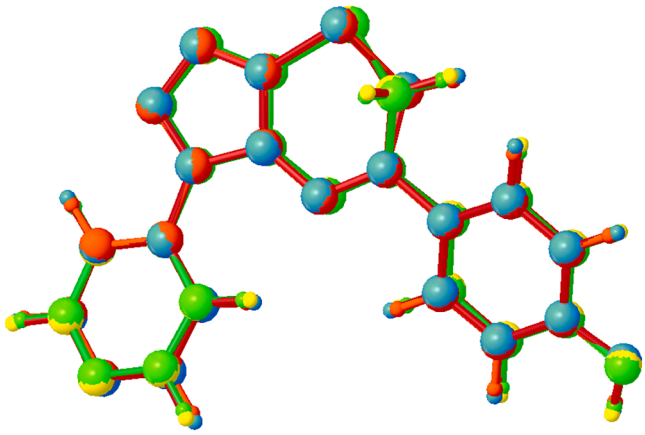

Fig. 9. The overlay of XRD (green and yellow) and DFT (red and blue) structures of PTTP dimer molecule.

3.3.4. Energy framework analysis

The three-dimensional topology of the interactions exhibited between the molecule responsible for the crystal packing are visualized in terms of the energy framework. The interaction energy components are, electrostatic (E_{ele}) (−173.45 kJ/mol), polarization (E_{pol}) (−53.57 kJ/mol), dispersion (E_{dis}) (−255.89 kJ/mol), repulsion (E_{rep}) (120.26 kJ/mol) and the total interaction energy (E_{tot}) (−362.66 kJ/mol) were computed by generating a molecular cluster of radius 3.8 Å around the single molecule along c-axis (Fig. 8). The corresponding geometry of the interacting molecules are given in Table 4. The dispersive energy is found to be dominant over the other interaction energies present in the molecule, and it contributes significantly to the overall stability of the crystal packing.

3.4. Quantum computational studies

3.4.1. Density functional theory

The ground state of the synthesized PTTP compound was optimized using DFT-B3LYP level of theory with 6–311++*G*(d,p) basis set. The XRD and DFT overlay structures with RMSD value of 0.736 Å (without inversion) and 0.605 Å (with inversion) is shown in the Fig. 9. The optimized geometrical parameters of theoretical (DFT) and SC-XRD values (bond length, bond angle and torsional angle) of the 2-MT showed good correlation and the geometrical parameters are provided in the Table S1, S2, S3} respectively. The corresponding correlation coefficients are found to be 0.999, 0.999 and 0.999 for bond length, bond angle and torsional angle respectively. The theoretically computed vibrational frequencies showed excellent agreement with the experimental spectra Fig. S4(a). The UV–vis spectra of the optimized structure was generated by employing the CAM-B3LYP functional at the 6–311+G (d,p) level basis set using the Time-dependent density functional theory (TD-DFT) approach with the conductor-like polarizable continuum model (CPCM) and the maximum absorption peak was observed at 315 nm Fig. S4(b).

3.4.2. Frontier molecular orbital energies

The behavior of the molecule is mostly determined by the frontier molecular orbitals. It is observed that the HOMO localized over the region of the triazole and pyridine ring, with the energy of −6.5906 eV. Whereas, the LUMO orbital, is found to be concentrated over the PTTP moelcule with the energy of −2.5290 eV, indicating a more electrophilic characteristic for the molecule. This results in an energy gap of 3.9685 eV, indicating moderate kinetic stability with possible moderate chemical reactivity ($\Delta E = E_{LUMO} - E_{HOMO}$). An electronegativity value of 4.7051 eV is obtained by combining the ionization potential (6.6894 eV) and electron affinity (2.7209 eV), indicating a significant propensity to attract electrons. The electronic system's stability is confirmed by the negative chemical potential (–4.7051 eV), and a balance between chemical reactivity and resistance to charge transfer is highlighted by the global hardness (1.9843 eV) and its reciprocal softness (0.5040 eV^{-1}). Additionally, the molecule is categorized as an excellent electrophile due to its strong electron-accepting capacity, shown by its electrophilicity index of 5.5785 eV. Significant polarity is indicated by the predicted dipole moment of 4.6560 D, which might affect the molecule's solubility and intermolecular interactions and increase its potential biological activity. The orbitals distribution on the molecule is shown in the Fig. 10(a) and the determined other electronic properties are provided in the Table 5.

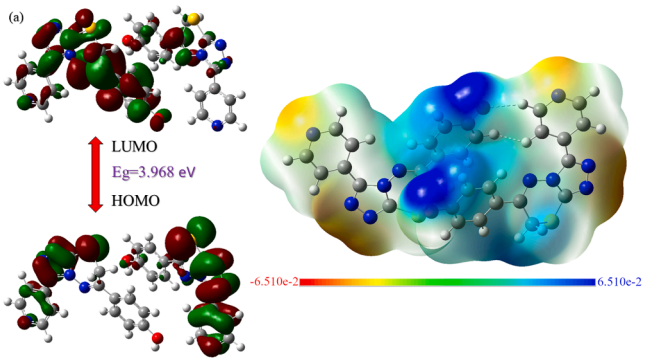

Fig. 10. Frontier molecular orbital distribution on the PTTP compound. Molecular electrostatic potential map of the PTTP compound revealing the electrophilic and nucleophilic regions.

Table 5
The HOMO-LUMO energy and quantum chemical parameters of the PTTP compound.

Parameter	Symbol and formula	Value
E_{HOMO}	E_H (eV)	−6.6894
E_{LUMO}	E_L (eV)	−2.7209
Energy gap (Eg)	$Eg=E_H - E_L$ (eV)	3.9685
Ionization energy (I)	$I=-E_H$ (eV)	6.6894
Electron Affinity (A)	$A=-E_L$ (eV)	2.7209
Electronegativity (χ)	$\chi=(1+A)/2$ (eV)	4.7051
Chemical Potential (μ)	$\mu=-\chi$ (eV)	−4.7051
Global hardness (η)	$\eta=\Delta E/2$ (eV)	1.9843
Global softness (σ)	$\sigma=1/2\eta$ (eV^{-1})	0.5040
Electrophilicity index (ω)	$\omega=\mu^2/2\eta$ ($eV^{}$)	5.5785
Dipole moment in Debye		4.6560

3.4.3. Molecular electrostatic potential

The MEP map is a visual aid for assessing the relative polarity and forecasting the molecule's reactive sites, or nucleophilic and electrophilic areas, which are connected to the electronic cloud. The PTTP molecule's MEP, which has a value of −7.832 e-2 a.u. (deep red), clearly shows the existence of a substantial negative potential with a red-colored area around nitrogen atoms (N3, N4, and N5) that are vulnerable to electrophilic attack. Additionally, it is discovered that the hydrogen atoms of the PTTP molecule, which have a value of +7.832 e-2 a.u. (deep blue), are home to the largest positive area. The triazole moiety's C—N group gives the terminal ring a rich yellow hue, but this is because the nitrogen atom is electronegative and may pull a lot of electrons away from the ring in the structure (Fig. 10(b)).

3.4.4. Fukui function

To examine the molecule's capacity to take part in the reaction, Fukui provided a general method based on the frontier orbital (FO) hypothesis [49]. It indicates whether an atom in a molecule is electrophilic or nucleophilic by describing the electronic density's propensity

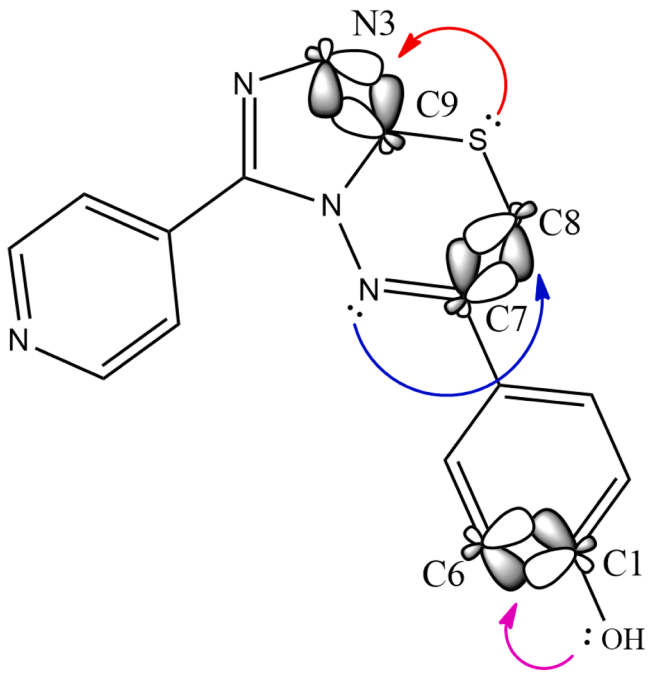

Fig. 11. The schematic representation of hyper conjugative interactions exhibited by the PTTP compound.

to deform at a specific location in order to donate or take an electron. A position is vulnerable to nucleophilic assault if $\Delta f(r) > 0$, and to electrophilic attack if $\Delta f(r) < 0$ [50,51]. Therefore, the Multiwfn program is used to determine the Fukui function values for the synthesized molecule (Table S4). From the calculated values, it is observed that the f^+ (reactive site for nucleophilic attack) value of the S1 atom is highest and it is most vulnerable to nucleophilic attack. And the f^- (reactive site for electrophilic attack) value for N4 is found to be the highest.

3.4.5. *Natural bond orbitals (NBO)*

The stabilization of the molecular structure was aided by hyper conjugative interactions such as π-π* and LP-π*, which are all determined to be related to *p* hybridization. It is found that the stabilization energy of the hyper-conjugative interaction resulting from the orbital overlap between the LP(1)-N2→π*(C9-N3), LP(1)-N2→π*(C10-N4), LP (1)-01→π*(C6-C1), LP(1)-S2→π*(C9-N3), having 40.33, 36.44, 28.26, 20.94 kcal/mol. The π(C11-C12) →π*(N5-C13), π(N5-C13→π*(C14-C15), π(C6-C1)→π*(C4-C5), π(C3-C2)→π*(C6-C1) with the stabilization energy 27.14, 25.14, 25.1 and 23.26 kcal/mol, respectively as listed in Table 6. These findings demonstrated the substantial interaction between electron donors and electron acceptors and, also intermolecular charge transfer mechanism in PTTP molecule as shown inFig. 11 and Table 6.

3.5. *Topology analysis*

3.5.1. *QTAIM and NCI-RDGanalysis*

The quantum theory of atoms in molecules (QTAIM) approach was employed for a better understanding of the electronic structure of the molecule. All the interactions were identified with the bond critical points (BCP) and bond paths (BP). The presence of a bond critical point between any two atoms shows that they are interacting and is an important indicator of bond strength. The BP referred to as the atomic interaction line in the topological study of the electron density ρ(r) distribution. This is the RDG based QTAIM analysis of the molecule PTTP.

The Fig. 12(a) indicates that in between the dimer molecule a large green patchy region was observed indicating the van der Waals type of interactions. It can be confirmed that along with the intra-molecular interactions there are inter-molecular interactions are present in the PTTP molecule, governed by the van der Waals type of interactions. The inter and intramolecular interactions such as C6-H6···S1B, C2-H2···C4B, C13-H13···O1B, C6B-H6B···N1, C12-H12···H6B, C8B-H8BA···H5B*, C12-H12···N1*, C12B-H12B···N1B*, C3···S6B* (* indicates intra molecular interactions) are observed in the molecular graph of the compound as shown in Fig. 12(a).

For intramolecular H-bonds, Table 7 provides the computed values of ρ(r), $\nabla^2\rho(r)$, H(r), G(r), V(r), H(r)/ρ(r), G(r)/ρ(r), and $-V(r)/G(r)$ at the BCPs. Chemical bonding and other hydrogen bonding interactions are explained by the Laplacian analysis. The weak and non-covalent character of the bonds is confirmed by the electron density $\nabla^2\rho(r)$, which provides evidence of charge concentration as depletion, $\nabla^2\rho(r) > 0$ in the bonding area. Stable bonding is indicated by H(r)>0. The polarization of the interaction was associated with the G(r)/ρ(r) ratio. Greater charge separation and, hence, less polarizability are associated with bigger G(r)/ρ(r) ratios. Table 7 lists the several topological

Table 6
Second-order perturbation theory analysis of Fock matrix carried using the NBO calculations.

Donor atoms	Occupancy	Hybridization	Acceptor atoms	Occupancy	Hybridization	$E^{(2)}$ kcal/mol
LP(1)-N2	1.562	N2 * p(99.06 %)	π*(C9-N3)	0.392	0.7540 * C9 p(99.86 %) -(−0.6670)* N3 p(99.81 %)	40.33
LP(1)-N2	1.566	N2 * p(99.06 %)	π*(C10-N4)	0.345	0.7533 * C10 p(99.82 %) -(−0.6576)* N4 p(99.79 %)	36.44
LP(2)-O1	1.863	O1 * p(99.94 %)	π*(C6-C1)	0.379	0.6800 * C6 p(99.98 %) -(−0.7332)* C1 p(99.95 %)	28.26
π(C11-C12)	1.632	0.7049 * C11 p(99.97 %) -(0.7094)* C12 p(99.95 %)	π*(N5-C13)	0.375	0.6434 * N5 p(99.87 %)- (−0.7655)* C13 p(99.87 %)	27.14
π(N5-C13)	1.715	0.7655 * N5 p(99.86 %) -(0.6434)* C13 p(99.87 %)	π*(C15-C14)	0.275	0.6930 * C15 p(99.95 %) -(−0.7210)* C14p (99.94 %)	25.14
π(C6-C1)	1.608	0.7332 * C6 p(99.95 %) -(0.6800)* C1 p(99.96 %)	π*(C4-C5)	0.409	0.6800 * C4 p(99.98 %) -(−0.7332)* C5 p(99.95 %)	25.1
π(C3-C2)	1.702	0.6760 * C3 p(99.94 %) -(0.7369)* C2 p(99.96 %)	π*(C6-C1)	0.379	0.6800 * C6 p(99.98 %) -(−0.7332)* C1 p(99.95 %)	23.26
π(C15–C14)	1.637	0.7210 * C15 p(99.95 %)-0.6930* C14 p(99.94 %)	π*(C11-C12)	0.366	0.7094 * C11 p(99.97 %) -(0.7049)* C12 p(99.95 %)	22.71
π(C4-C5)	1.643	0.7332 * C4 p(99.98 %) - 0.6800* C5 p(99.95 %)	π*(C3-C2)	0.305	0.7369 * C3 p(99.94 %) -(−0.6760)* C2 p(99.96 %)	21.71
LP(2)-S1	1.839	S1 p(99.92 %)	π*(C9–N3)	0.392	0.7540 * C9 p(99.86 %) -(−0.6670)* N3 p(99.81 %)	20.94

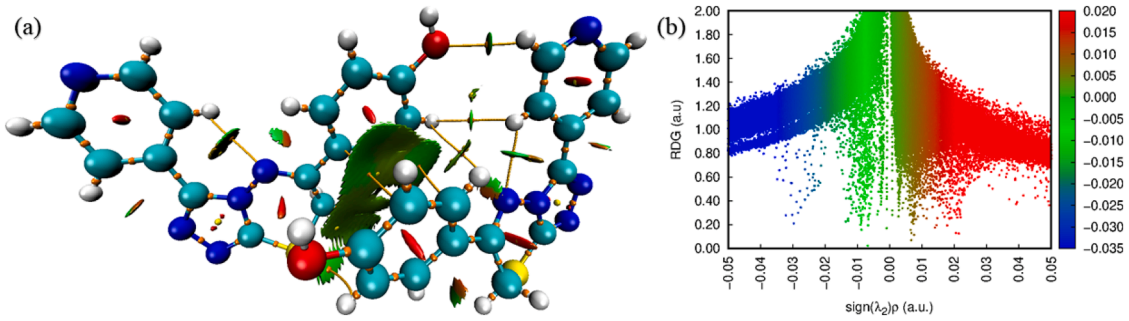

Fig. 12. (a) The molecular graph of the molecule revealing the intramolecular interactions associated with the bond critical points. (b) Non-covalent interaction (NCI) analysis of the synthesized molecule obtained using the electron densities. NCI isosurface for compound with isovalue = 0.2 a.u. (left) and reduced density gradient-based 2D scatter plot (right).

Table 7
Various topological parameters at BCPs for PTTP molecule.

Type of interaction	ρ(r)	$\nabla^2\rho(r)$	V(r)	G(r)	H(r)	H(r)/ρ(r)	G(r)/ρ(r)	-V(r)/G(r)
C6-H6···S1B	0.00279	0.00823	−0.00098	0.00152	0.00053	0.18996	0.54480	0.6447
C2-H2···C4B	0.00343	0.00911	−0.00155	0.00191	0.00036	0.10495	0.55685	0.1884
C13-H13···O1B	0.00947	0.03427	−0.00572	0.00714	0.00142	0.14994	0.75395	0.8011
C6B-H6B···N1	0.00214	0.00777	−0.00100	0.00147	0.00046	0.21495	0.68691	0.6910
C12-H12···H6B	0.00340	0.01165	−0.00175	0.00233	0.00057	0.16764	0.68529	0.7510
C8B-H8BA···H5B*	0.01345	0.06257	−0.00911	0.01237	0.00326	0.24237	0.91970	0.7364
C12-H12···N1*	0.01142	0.04238	−0.00671	0.00865	0.00193	0.16900	0.75744	0.7757
C12B-H12B···N1B*	0.01464	0.05597	−0.00888	0.01143	0.00255	0.17418	0.78073	0.7769
C3···S6B*	0.00462	0.0119	−0.00189	0.00243	0.00054	0.11688	0.52597	0.7777

Where ρ(r) is the electron density, $\nabla^2\rho(r)$ is the Laplacian electron density, V(r) is the potential energy density, G(r) is the Lagrangian kinetic energy density, and H(r) is the total energy density (all the units are in a.u).

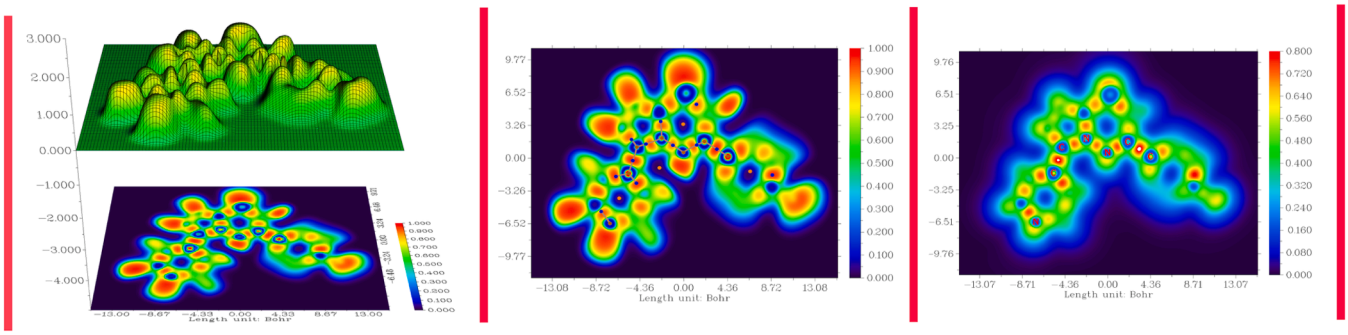

(a) Color filled and contour maps of the electron localization **(b) Localized orbital locator**

Fig. 13. Color filled maps and contour maps of the ELF and LOL of the compound.

characteristics of the compound that were determined at the BCPs. With all units in a. u., the electron density is denoted by ρ(r), the Laplacian electron density by $\nabla^2\rho(r)$, the potential energy density by V(r), the Lagrangian kinetic energy density by G(r), and the total energy density by H(r). As you can observe in the 2D scatterplot shown in the Fig. 12(b), large number of green colored peaks were observed between 0.01 to −0.02. So, this indicates or this corroborates the findings that we have seen in the Fig. 12(a) that is NCI based RDG isosurface plot, further justifies that the dimer molecule is interacting with each other through van der Waals type of interaction as seen by the green colored region present in between the two molecules.

3.5.2. *Electron localization function and localized orbital locator*

The molecular structure and electron density distribution are directly related, as demonstrated by the electron localization function and localized orbital locator analysis based on the quantum chemical postulates. The covalent bond reactivity, shell structure, surface analysis, and aromaticity of the synthesized compound PTTP were ascertained using the relief map of the electron localization function. Whereas the blue region surrounding the nitrogen atom suggests the existence of delocalized electrons, the red region surrounding the hydrogen and carbon atoms is indicative of localized electrons.

The electron depletion zone between the valence and inner shells of the carbon atoms in the molecule is shown by dark blue rings around the nuclei, while the atoms' nuclei are represented by the red color ring. The electron depletion area between the inner and valance shells is depicted by the blue circles around the lone pair of nitrogen and sulfur atoms (N1, N2, N5, and S1) (Fig. 13(a)). While the high LOL values of the covalent kind of electron depletion region around the nitrogen atom are shown in red, the valence shell of the depleted zone and the inner shells of bromine and a few carbon nuclei are each shown by blue color regions [47]. Fig. 13 displays the PTTP molecule's LOL and ELF.

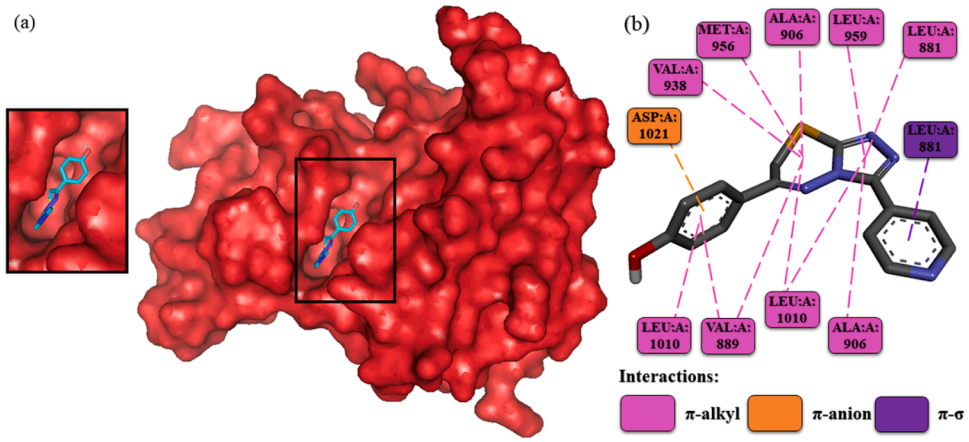

Fig. 14. (a) Surface view of the docking of the ligand (PTTP) with *JAK2* protein, (b) 2D interaction diagram revealing various interactions between the ligand and the protein.

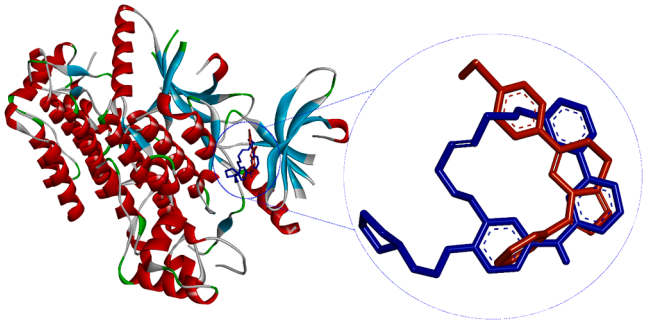

Fig. 15. Cartoon view of the docking of the combined ligand PTTP (brown colour) and standard drug pacritinib (blue colour) with JAK2 protein.

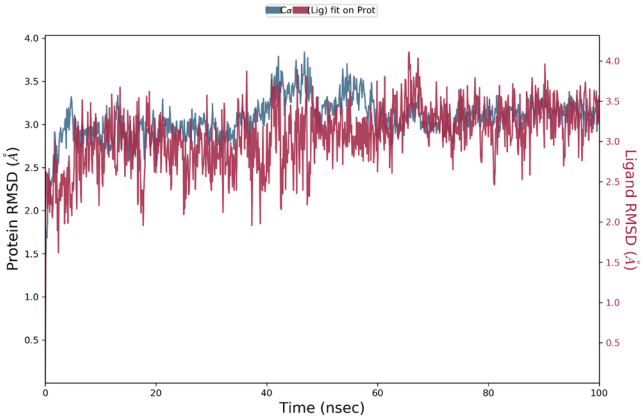

Fig. 16. The RMSD plot of PTTP compound with 3EYH protein during the course of 100 ns simulation.

4. *In-silico* studies

4.1. Molecular docking studies

The protein-ligand (*JAK2*-PTTP compound) interaction plays a significant role in structurebased drug designing and discovery process through molecular docking studies, which is used in this work to assess how well the PTTP compound attach to the coordinates of kinase domain of *Janus tyrosine kinase 2* (*JAK2*). The best docking pose with corresponding interactions are shown in the Fig. 14(a). The molecular docking results indicated a good binding score of −9.5 kcal/mol with the *JAK2* protein. It is observed that PTTP interacts with seven favourable residues (ASP1021, VAL938, MET956, ALA906, LEU959, LEU881, ALA906, LEU1010, VAL889, LEU1010) of the JAK2 protein (Fig. 14(b)). The PTTP forms following considerable zones of inhibition against the amino acids of the JAK2 protein, π-anion stacks via ASP; A1021 (aspartic acid with the π-anion bond of phenyl moiety), The π −σ bond via LEU; A881 (leucine interaction via the π−σ bond with pyridine ring). The π-alkyl interactions via VAL938, MET956, ALA906, VAL889, LEU1010 are interacting with the thidiazene ring, in addition to these LEU; A959, LEU; A881, LEU; A1010, ALA; A906 are also interacting with the PTTP molecule through π-alkyl interaction with the triazole moiety, further the amino acid residues LEU; A1010 and VAL; A889 are also interacting with the phenyl ring of the PTTP molecule through the same type interaction as shown in the Fig. 14(b). The molecular docking results of PTTP was compared with standard medication drug named pacritinib (Fig S-7) and interestingly, both the compounds showed similar amino acid interactions against the JAK2 protein. The Fig 15 reveals superimpose of both the compounds (PTTP and pacritinib) indicating the presence of the PTTP molecule in the similar active region of the pacritinib. The amino acids interacting with both the compounds are given in the Table S5.

4.2. Molecular simulation studies

To study the movement of molecules with protein, dynamic simulation was carried out. The RMSD was considered to predict the degree

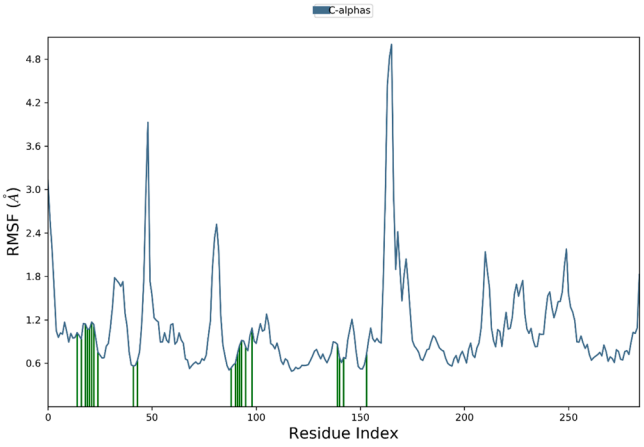

Fig. 17. P-RMSD plot of PTTP compound with 3EYH protein during the course of 100 ns simulation.

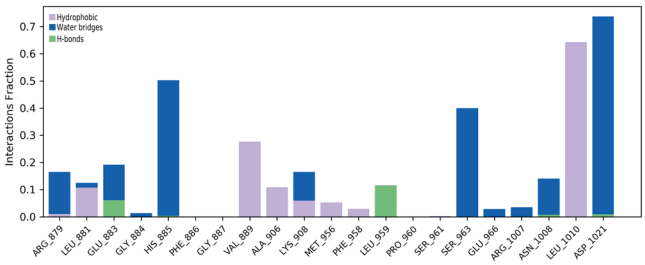

Fig. 18. The ligand protein contact (PDB ID: 3EYH) map revealing the percentage contribution of the amino acid with the ligand.

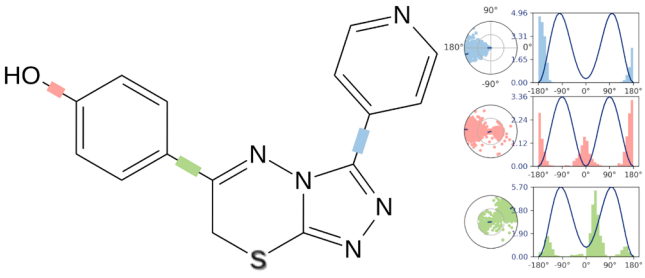

Fig. 19. Torsional profile of PTTP compound during the simulation period of 100 ns.

of deviation in the initial structure during the simulation time. The RMSD plot of the protein-PTTP ligand system shows, well, the deviation of the protein and ligand below 3.5 Å Notably, the behaviour of the protein doesn't make any more considerable changes with the presence of ligand binded to the active region. In the Fig. 16 we observe the results of 100 ns MD simulation revealed a small deviation will be there in the initial period. After 5 ns, the protein-ligand complex reaches the equilibrium state until the end of the simulation period indicates the ligand highly stable in the active pocket of the protein. During the simulation period, the fluctuations of amino acids of protein with the ligand PTTP are shown in the Fig. 17. The fluctuations of amino acid interactions with the ligand are shown as ASP866 (3.16 Å), GLU897 (1.94 Å), PRO912 (2.56 Å), LYS1035 (5.32 Å), ASP1042 (3.42 Å), GLN1098 (2.16 Å), ASN1119 (2.19 Å), ARG1007 (1.01 Å). The duration time for the amino acids in interactions of the protein with the ligand reveals hydrophobic interactions such as ARG 879 (17.2 %), LEU 881 (12.5 %), LEU1010 (56.9 %), VAL889 (33.0 %), ALA906 (6.9 %), LYS908 (11.3 %), MET956 (3.7 %), PHE958 (4.7 %). The water brides are observed in the amino acids of ASP1021 (76.8 %), HIS885 (50.2 %), ASN1008 (9.1 %), SER963 (24.4 %), LYS908 (5.4 %), GLY884(1.6 %), GLU883 (16.6 %), ARG879 (17.2). The few of amino acids are involved in hydrogen bond interaction they are LEU 959(13.5 %) and GLU883 (12.5 %) shown in Fig. 18. The torsional plot of the PTTP ligand describes that there exist three rotational bonds indicated by the green, red and blue colour. Further, the degree with which the rotation of the bonds happens is shown in the dial plots as shown in the Fig. 19. The RMSD and rGyr plot of the PTTP compound showed the value to be averaged at 0.5, 3.7 Å respectively. No intramolecular hydrogen bond formation was observed. Further, the MolSA, SASA and PSA properties of the compound are found to be 276, 75 and 133 $Å^2$ respectively as shown in Fig. 20.

5. Conclusion

In summary, the compound 4-[3-(pyridin-4-yl)-7H-[1,2,4]triazolo [3,4-b][1,3,4]thiadiazin-6-yl]phenol (PTTP) was successfully synthesized and structurally characterized. Single-crystal X-ray diffraction analysis revealed that the molecule crystallizes in the monoclinic crystal system with $P2_1/c$ space group, confirming its three-dimensional molecular arrangement and crystal packing via C13B-H13B···O1 and O1-H1···N5B interactions. DFT studies revealed that HOMO–LUMO energy gap of 3.968 eV, suggesting good chemical stability with potential

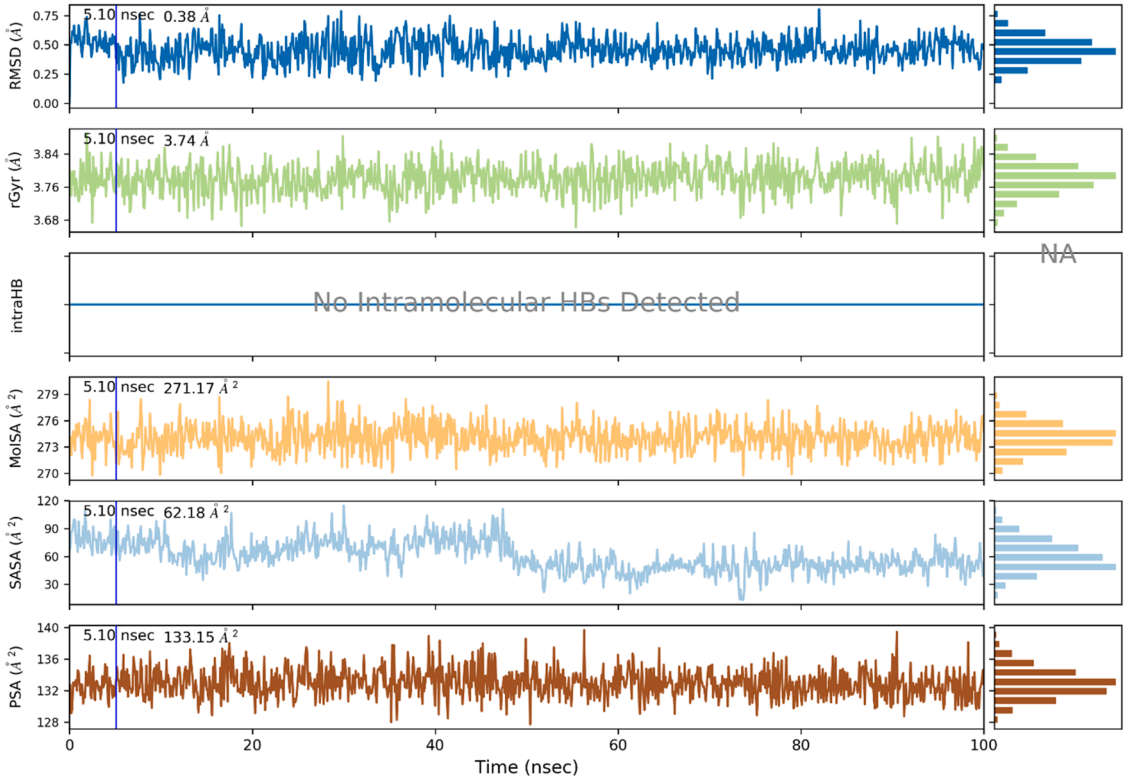

Fig. 20. Study of the various properties of PTTP compound during the simulation period of 100 ns.

electronic transitions. Complementary analyses, including MEP mapping, NBO analysis, non-covalent interaction (NCI)–based RDG, and QTAIM analysis, provided deeper understanding of the electronic distribution, intramolecular charge transfer, and the role of non-covalent interactions in stabilizing the molecule. The molecular docking study against JAK2 protein demonstrated a favorable binding affinity with a binding energy of –9.5 kcal/mol, supported by π-alkyl, π-anion and π−σ interactions within the active site. Additionally, the compound's potential as a promising JAK2 inhibitor has been confirmed by molecular dynamics (MD) simulations, which verified the stability of the protein–ligand complex under physiological settings. The pharmacological significance of this triazolothiadiazole derivative is generally well supported by the combined experimental and theoretical studies, which also offer a solid basis for its future advancement as a therapeutic lead.

Supporting information

CCDC-2203513 contains the supplementary crystallographic data for this paper. These data can be obtained free of charge via https://www.ccdc.cam.ac.uk/structures/, or by e-mailing mailto:data_request@ccdc.cam.ac.uk, or by contacting The Cambridge Crystallographic Data centre, 12 Union Road, Cambridge CB2 1EZ, UK; fax: +44(0) 1223–336,033.

CRediT authorship contribution statement

D.C. Vinay Kumar: Writing – original draft, Visualization, Software, Methodology, Investigation, Formal analysis, Data curation, Conceptualization. **B.S. Chethan:** Writing – original draft, Validation, Supervision, Software, Methodology, Investigation, Formal analysis, Data curation, Conceptualization. **S. Neetha:** Visualization, Resources, Investigation, Funding acquisition, Formal analysis, Conceptualization. **Darshini Gowda:** Visualization, Validation, Resources, Formal analysis, Conceptualization. **V. Shalini:** Methodology, Investigation, Formal analysis, Data curation, Conceptualization. **T.N. Lohith:** Writing – original draft, Visualization, Funding acquisition, Formal analysis, Conceptualization. **K.S. Rangappa:** Writing – review & editing, Validation, Supervision, Resources, Project administration, Investigation, Conceptualization. **N.K. Lokanath:** Writing – review & editing, Supervision, Resources, Project administration, Methodology, Funding acquisition, Conceptualization.

Declaration of competing interest

The authors declare that they have no known competing financial interests or personal relationships that could have appeared to influence the work reported in this paper.

Acknowledgment

Vinay Kumar D. C. Thank NIE-CRD, The National Institute of Engineering, Mysuru for the providing the financial assistance. Rangappa K. S. thanks to Indian Science congress for providing Asutosh Mookerjee fellowship (Grant No.: 595/ 73/2020–21), CSIR for emeritus fellowship (Grant No 21(1117)/ 20/EMR-II) and NASI Distinguished chair Professor (Grant No.: NASI/2025/07/Fellowship/89). We are also thankful to the institution of excellence (IOE), University of Mysore, Manasagangotri, Mysuru-570006, India, for the spectral data and Dr. Sridhar Balasubramanian, Principal scientist, Centre for X-ray Crystallography, CSIR Indian Institute of chemical technology (IICT), Hyderabad-500007, India for X-ray crystallographic data. CPEPA, IOE and DST-PURSE-II, Vijnana Bhavan, University of Mysore, Mysuru.

Supplementary materials

Supplementary material associated with this article can be found, in the online version, at doi:10.1016/j.molstruc.2025.144689.

Data availability

Data will be made available on request.

References

[1] M.M. Kamel, N.Y.M. Abdo, Synthesis of novel 1,2,4-triazoles, triazolothiadiazines and triazolothiadiazoles as potential anticancer agents, Eur. J. Med. Chem. 86 (2014) 75–80.
[2] C. Kamoutsis, M. Fesatidou, A. Petrou, A. Geronikaki, V. Poroikov, M. Ivanov, P. Mladënka, Triazolo based-thiadiazole derivatives: synthesis, biological evaluation and molecular docking studies, Antibiotics 10 (2021) 804.
[3] I. Khan, A. Ibrar, N. Abbas, Triazolothiadiazoles and triazolothiadiazines – Biologically attractive scaffolds, Eur. J. Med. Chem. 63 (2013) 854–868.
[4] N.K. Mothahalli Raju, B. Paul, L. Tn, S. Bodduna, N.K. Kandukuri, Sulfur-controlled modulation of peptoid atropisomeric foldamers, J. Org. Chem. 90 (2025) 4796–4807.
[5] R.M. Abdelhameed, H.A. El-Sayed, M. El-Shahat, A.A. El-Sayed, O.M. Darwesh, Novel triazolothiadiazole and triazolothiadiazine derivatives containing pyridine moiety: design, synthesis, bactericidal and fungicidal activities, Curr. Bioact. Compd. 14 (2018) 169–179.
[6] L. Maji, S. Sengupta, G.S. Purawarga Matada, G. Teli, G. Biswas, P.K. Das, M. P. Mudgal, Medicinal chemistry perspective of JAK inhibitors: synthesis, biological profile, selectivity, and structure activity relationship, Mol. Divers. 28 (2024) 4467–4513.
[7] L. Chen, Y. Hu, Z. Lu, Z. Lin, L. Li, J.Q. Wu, J. Hu, Design, synthesis, and antitumor efficacy of substituted 2-amino[1,2,4]triazolopyrimidines and related heterocycles as dual inhibitors for microtubule polymerization and Janus kinase 2, J. Med. Chem. 66 (2023) 15006–15024.
[8] M.M. Kamel, N.Y.M. Abdo, Synthesis of novel 1,2,4-triazoles, triazolothiadiazines and triazolothiadiazoles as potential anticancer agents, Eur. J. Med. Chem. 86 (2014) 75–80.
[9] C. Kamoutsis, M. Fesatidou, A. Petrou, A. Geronikaki, V. Poroikov, M. Ivanov, P. Mladënka, Triazolo based-thiadiazole derivatives: synthesis, biological evaluation and molecular docking studies, Antibiotics 10 (2021) 804.
[10] X.Q. Deng, Z.Q. Dong, M.X. Song, B. Shu, S.B. Wang, Z.S. Quan, Synthesis and anticonvulsant activities of some triazolothiadiazole derivatives, Arch. Pharm. 345 (2012) 565–573.
[11] A. Husain, M.A. Naseer, M. Sarafroz, Synthesis and anticonvulsant activity of some novel fused heterocyclic 1,2,4-triazolo[3,4-b]-1,3,4-thiadiazole derivatives, Acta Pol. Pharm. 66 (2009) 135–140.
[12] B. Hazarika, L. Ropuia, V.P. Singh, Biological relevance and applications of triazolothiadiazole exploring interactions, synthesis, and mechanisms: structural study of triazolothiadiazoles. Examining Biological Relevance of Fused S-Heterocycles, IGI Global Scientific Publishing, 2025, pp. 33–70.
[13] A.T. Boraei, H.A. Ghabbour, M.S. Gomaa, E.S.H. El Ashry, A. Barakat, Synthesis and anti-proliferative assessment of triazolo-thiadiazepine and triazolo-thiadiazine scaffolds, Molecules. 24 (2019) 4471.
[14] M. Sarafroz, Y. Khatoon, M. Amir, M. Taleuzzaman, C. Yadav, Synthesis, spectral characterization and anticonvulsant studies of the novel triazolothiadiazoles bearing benzoxazole moiety, Orient. J. Chem. 37 (2021).
[15] D.K. Nancy, A. Soam, A review on anti-bacterial activity of substituted azetidinone, benzothiazole, thiazole, thiadiazole, triazole, triazolothiazole and naphthalene derivatives, J. Survey Fish. Sci. 8 (2022) 634–675.
[16] B. Hazarika, L. Ropuia, V.P. Singh, Biological relevance and applications of triazolothiadiazole exploring interactions, synthesis, and mechanisms: structural study of triazolothiadiazoles. Examining Biological Relevance of Fused S-Heterocycles, IGI Global Scientific Publishing, 2025, pp. 33–70.
[17] A. Tefferi, T. Barbui, Bcr/abl-negative, classic myeloproliferative disorders: diagnosis and treatment, Mayo Clin. Proc. 80 (9) (2005) 1220–1232.
[18] K.K. Ballen, S. Shrestha, K.A. Sobocinski, M.-J. Zhang, A. Bashey, B.J. Bolwell, F. Cervantes, S.M. Devine, R.P. Gale, V. Gupta, Outcome of transplantation for myelofibrosis, Biol. Blood Marrow TransPlant 16 (2010) 358–367.
[19] J. Mascarenhas, E. Virtgaym, M. Stal, H. Blacklock, A.T. Gerds, R. Mesa, P. Ganly, D. Snyder, I. Tabbara, D. Tremblay, Outcomes of patients with myelofibrosis treated with compassionate use pacritinib: a sponsor-independent international study, Ann. Hematol. 97 (2018) 1369–1374.
[20] H. Hamaguchi, Y. Amano, A. Moritomo, S. Shirakami, Y. Nakajima, K. Nakai, N. Nomura, M. Ito, Y. Higashi, T. Inoue, Discovery and structural characterization of peficitinib (ASP015K) as a novel and potent JAK inhibitor, Bioorg. Med. Chem. 26 (2018) 4971–4983.
[21] T.N. Lohith, B.H. Gayathri, M. Feizi-Dehnayebi, S. Kumar, K. Divya, M.A. Sridhar, G.M. Ziarani, In-silico studies of 3-tert-butyl-7-[2-phenyl ethenyl]-4H-[1,3,4] thiadiazolo[2,3-c][1,2,4]triazin-4-one as a potential SARS-CoV-2 inhibitor: insights from an experimental and computational approach, J. Mol. Struct. 1330 (2025) 141356.
[22] S. Kumar, K. Divya, M. Sridhar, M. Mahendra, A new thiadiazole-triazine derivative: structural investigation, DFT studies, ADME-T analysis and SARS-CoV-2 activity by docking simulation, J. Mol. Struct. 1317 (2024) 139133.
[23] V. Shalini, A.N. Priyadarshini, B. Harsha Kachigere, D.C. Vinay Kumar, B. S. Chethan, M.S. Sudhanva, S.R. Kanchugarakoppal, Novel quinoline-4-carboxamide derivatives potentiate apoptosis by targeting PDK1 to overcome

chemo-resistance in colorectal cancer: theoretical and experimental results, Heliyon. 10 (2024) e219.
[24] S. Neetha, C. Santhosh, D.V. Kumar, T.N. Lohith, K. Pruthviraj, K. Sunil, S. K. Verma, Synthesis, structure elucidation, DFT, molecular docking studies, and antioxidant activities of thiazole derivative: a combined experimental and computational study, J. Mol. Struct. (2025) 143430.
[25] T.N. Lohith, S. Neetha, V.H. Kameshwar, K.S.S. Kumar, M.S. Ali, H.A. Al-Lohedan, S.K. Verma, Structural analysis and computational studies of pyrazole derivative: investigation of interactions by X-ray crystallography, DFT, molecular docking, and molecular dynamics simulation, J. Mol. Struct. (2025) 143497.
[26] D. Rekharani, V.K. DC, B.S. Chethan, D. Urs, K.R. Sathisha, N.K. Lokanath, S. Naveen, Exploration of crystal structure, supramolecular organization, and computational studies of a novel pyrazole derivative: a structural and theoretical perspectives, J. Mol. Struct. 1321 (2025) 140265.
[27] C.C.S. Rigaku, Expert 2.0 r15, Software for Data Collection and Processing, Rigaku Corporation, Tokyo, Japan, 2011.
[28] G.M. Sheldrick, A short history of SHELX, Acta Crystallogr. A 64 (2008) 112–122.
[29] G.M. Sheldrick, Crystal structure refinement with SHELXL, Acta Crystallogr. C 71 (2015) 3–8.
[30] A.L. Spek, Structure validation in chemical crystallography, Acta Crystallogr. D 65 (2009) 148–155.
[31] C.F. Macrae, I. Sovago, S.J. Cottrell, P.T. Galek, P. McCabe, E. Pidcock, P.A. Wood, Mercury 4.0: from visualization to analysis, design and prediction, J. Appl. Crystallogr. 53 (2020) 226–235.
[32] M.A. Spackman, D. Jayatilaka, Hirshfeld surface analysis, CrystEngComm. 11 (2009) 19–32.
[33] A. Bhattacharjee, S. Hegde, A.M. Kurumbala, V. Kumar, N. Honnappa, M.S. Ali, M. M. Reddy, Structural elucidation, Hirshfeld surface analysis, DFT, and molecular docking studies of puckered compound: (6aS,12aR)-9-bromo-7,7-dimethyl-6a,7,12,12a-tetrahydro-6H,13H-thiochromeno[3′,4′:5,6]thiopyrano[4,3-b] quinoline, J. Mol. Struct. 1338 (2025) 142135.
[34] V. Shalini, D.V. Kumar, D. Gowda, B.S. Chethan, B.K. Harsha, S.M. Rajesh, K. S. Rangappa, Unveiling the structural and theoretical properties of 6-(2-fluoro-3-methylpyridin-4-yl)-2-(4-methoxyphenyl)-N-phenylquinoline-4-carboxamide compound as Sonic Hedgehog protein inhibitor: synthesis, SCXRD, HSA, DFT, docking and ADMET studies, J. Mol. Struct. 1330 (2025) 141495.
[35] J. Tirado-Rives, W.L. Jorgensen, Performance of B3LYP density functional methods for a large set of organic molecules, J. Chem. Theory. Comput. 4 (2008) 297–306.
[36] M.P. Andersson, P. Uvdal, New scale factors for harmonic vibrational frequencies using the B3LYP density functional method with the triple-ζ basis set 6-311+G(d, p), J. Phys. Chem. A 109 (2005) 2937–2941.
[37] M.J. Frisch, G.W. Trucks, H.B. Schlegel, G.E. Scuseria, M.A. Robb, J.R. Cheeseman, D.J. Fox, Gaussian 16 Revision C.01, Gaussian Inc., Wallingford CT, 2016.
[38] R.D. Dennington, T.A. Keith, J.M. Millam, GaussView 5.0.8, Gaussian Inc., 2008.
[39] D. Rekharani, V.K. DC, B.S. Chethan, D. Urs, N.K. Lokanath, S. Naveen, Design, structural characterization, computational techniques, and in-silico assessment of 6-chloro-2-(3-chloro-1-(3-chloropyridin-2-yl)-1H-pyrazol-5-yl)-8-methyl-4H-benzo [d][1,3]oxazin-4-one offering a promising antagonist of the deadly coronavirus main protease, coupled with pharmacokinetic profiles and drug-like characteristics, J. Mol. Struct. (2025) 143390.
[40] P.S. Pradeep Kumar, K. Sunil, B.S. Chethan, N.K. Lokanath, N. Madan, A.M. Sajith, Synthesis, characterisation, biological and theoretical studies of novel pyridine derivatives, Mol. Phys. 120 (2022) e2093283.
[41] T. Lu, F. Chen, Multiwfn: a multifunctional wavefunction analyzer, J. Comput. Chem. 33 (2012) 580–592.
[42] R.F.W. Bader, Atoms in Molecules: A Quantum Theory, Clarendon Press, Oxford, 1994.
[43] R.F. Bader, Bond paths are not chemical bonds, J. Phys. Chem. A 113 (2009) 10391–10396.
[44] G.M. Morris, R. Huey, W. Lindstrom, M.F. Sanner, R.K. Belew, D.S. Goodsell, A. J. Olson, AutoDock4 and AutoDockTools4: automated docking with selective receptor flexibility, J. Comput. Chem. 30 (2009) 2785–2791.
[45] Discovery Studio Modeling Environment, Dassault Systèmes BIOVIA, San Diego, 2017.
[46] F. Xue, H.D. Preetham, R. Verma, T.N. Lohith, S. Raju, M.S. Ali, V.H. Kameshwar, Structure-property relationship of two gamma-lactam derivatives: hirshfeld surface analysis, DFT, and molecular dynamics simulations, Chem. Phys. Lett. 857 (2024) 141725.
[47] A.K. Tonduru, Computational exploration of OATP substrate binding and transport dynamics (2025).
[48] D.J. Cole, J. Tirado-Rives, W.L. Jorgensen, Molecular dynamics and Monte Carlo simulations for protein–ligand binding and inhibitor design, Biochim. Biophys. Acta Gen. Subj. 1850 (2015) 966–971.
[49] K. Fukui, Role of frontier orbitals in chemical reactions, Science (1979) 218 (1982) 747–754.
[50] P. Geerlings, E. Chamorro, P.K. Chattaraj, F. De Proft, J.L. Gázquez, S. Liu, P. Ayers, Conceptual density functional theory: status, prospects, issues, Theor. Chem. Acc. 139 (2020) 36.
[51] S. Uzun, Z. Esen, E. Koç, N.C. Usta, M. Ceylan, Experimental and density functional theory (MEP, FMO, NLO, Fukui functions) and antibacterial activity studies on 2-amino-4-(4-nitrophenyl)-5,6-dihydrobenzo[h]quinoline-3-carbonitrile, J. Mol. Struct. 1178 (2019) 450–457.